

1
2 **Projections of future hydrologic drought in a reservoir-regulated region: the role of**
3 **climate change and reservoir operation**

4
5 **Shaokun He^{1,5}, Sirui Sun², Yanghe Liu³, Keping Chen^{4*}, Lingling Zhu⁴, Yu Gong^{1*}**

6 ¹State Key Lab. of Water Resources Engineering & Management, Wuhan University, Wuhan
7 430072, China.

8 ²Middle Changjiang River Bureau of Hydrology and Water Resources Survey, Bureau of
9 Hydrology of Changjiang Water Resources Commission, Wuhan 430010, China.

10 ³Three Gorges Cascade Dispatch & Communication Center, China Yangtze Power Co., Ltd.,
11 Yichang 443000, China

12 ⁴Bureau of Hydrology of Changjiang Water Resources Commission, Wuhan 430010, China.

13 ⁵Department of Physical Geography and Ecosystem Science, Lund University, Lund 223 62,
14 Sweden

15

16 *Corresponding authors: chenkb@whu.edu.cn; ygong@whu.edu.cn

17

18

19 **Abstract**

20 Future hydrological droughts in reservoir-regulated regions remain unclear due to the
21 complex interactions between climate change and reservoir operation. Existing studies usually rely
22 on simplified empirical assumptions of historical reservoir operations and rarely consider the role
23 of optimal reservoir operation policies. Here, we used the upper Hanjiang River basin (UHRB) in
24 China as a case study to project its future hydrological drought evolution using standard
25 streamflow indices (i.e., SSI-1, SSI-3, and SSI-12) and to quantify the role of climate change and
26 reservoir operation. A long and short-term memory (LSTM)-based hydrological model, coupled
27 with a physics-informed LSTM reservoir model, is developed and driven by bias-corrected climate
28 outputs from five global climate models to project future drought conditions under three scenarios
29 (SSP126, SSP370, and SSP585). The results indicate that future climate change over the UHRB
30 tends to reduce natural streamflow and exacerbate hydrological droughts, with the most severe
31 impacts projected in the far-future period (2071-2100) under SSP585. The traditional Ankang
32 Reservoir operation reduces the frequency, duration and severity of short-term hydrological
33 droughts (SSI-1 and SSI-3) under all scenarios, but shows limited effectiveness for long-term
34 droughts (SSI-12). Importantly, optimal reservoir operating policies that aim to maximize
35 hydropower generation and power generation guarantee rate highlight clear trade-offs between
36 hydrological drought risk and hydropower benefits, thereby underscoring the importance of
37 enhancing reservoir operation strategies for future drought management in reservoir-regulated
38 basins.

39
40 **1 Introduction**

41 Hydrological droughts, characterized by abnormally low streamflow in rivers, have
42 significant direct and indirect ramifications on hydrological, agricultural, and socio-economic

43 sectors, such as losses of crops and hydropower generation (Chang et al., 2025; Ji et al., 2023;
44 Kheyruri et al., 2023). In recent decades, hydrological droughts have become more frequent in the
45 Americas, East Asia, Africa, and Oceania, and global warming arising from high greenhouse gas
46 concentrations has been identified as the main driver (Gudmundsson et al., 2021). According to
47 the Sixth Assessment Report (AR6) of the Intergovernmental Panel on Climate Change (IPCC,
48 2021), land temperatures are projected to continue to rise, which is expected to exacerbate extreme
49 hydrological droughts in a warming future. Hence, it is of great importance to assess the
50 characteristics of extreme hydrological droughts in the context of climate change to enable
51 effective adaptation strategies.

52 At the same time, the rapid global expansion of reservoirs as a major manifestation of
53 human intervention in river systems has introduced new challenges for assessing future
54 hydrological droughts. Currently, more than 55,000 reservoirs have been registered by the
55 International Commission on Large Dams, with a total storage capacity of 14,602 km³ (Eriyagama
56 et al., 2020). Such an extensive storage capacity suggests that reservoirs can substantially affect
57 hydrological drought characteristics by regulating the spatiotemporal distribution of river flows
58 (Ho and Ehret, 2025; G. Ribeiro Neto et al., 2023). From the perspective of hydraulic regulation
59 alone, reservoirs are often found to dampen low-flow extremes in strongly regulated river basins,
60 particularly in Europe and North America, thereby alleviating drought severity during dry seasons
61 (Wanders and Wada, 2015). However, reservoirs also enable intensified consumptive water use,
62 including irrigation expansion and other anthropogenic withdrawals, which may counteract or
63 even outweigh the buffering effects of flow regulation. For example, Wan et al. (2018) reported
64 that irrigation reservoirs could increase the duration and intensity of global hydrological droughts
65 by up to 50% during 2070–2099, largely due to enhanced water abstractions. Consequently, the

66 net impact of reservoir operation on future hydrological droughts is highly region-dependent,
67 reflecting the combined effects of hydraulic regulation, reservoir-enabled water use, and the
68 heterogeneity of regional climate change.

69 Recently, some scholars have begun such drought analysis efforts in some key watersheds
70 (Sun et al., 2023; Zhang et al., 2025; Cheng et al., 2024). Yun et al. (2021b) attempted to assess
71 the effectiveness of reservoir operation in modifying hydrological extremes in the Lancang-
72 Mekong River basin using five global climate models (GCMs) from the sixth Coupled Model
73 Intercomparison Project (CMIP6) and the VIC-Reservoir model. Ji et al. (2023) projected
74 hydrological drought changes in the upper Yellow River basin under different levels of global
75 warming by driving a hybrid Conjunctive Surface-Subsurface Process Version 2 (CSSPV2)
76 hydrological model coupled with a conceptual reservoir model derived from Hanasaki et al. (2006),
77 in which reservoir operations were represented using a generic rule-based formulation with
78 empirically calibrated parameters. These drought experiments demonstrated the feasibility of
79 coupling hydrological and reservoir modules for such problems, but their conclusions may remain
80 sensitive to empirical assumptions about reservoir releases when observed operating records (i.e.,
81 inflow/outflow/storage time series) are not explicitly used to constrain or evaluate the operating
82 representation. As one of the most influential human-engineered interventions under a changing
83 climate, reservoir systems warrant particular attention regarding the extent to which realistic
84 operating patterns can sustain system performance under plausible future scenarios (Culley et al.,
85 2016). Historical operating records contain rich decision-making information that reflects how
86 operators have adapted release strategies to diverse inflow conditions (Zheng et al., 2022).
87 Therefore, state-of-the-art tools that can systematically learn from long-term historical operating

88 records during periods with relatively stable objectives and constraints are critical for capturing
89 drought-relevant reservoir releases.

90 Against this background, machine learning (ML) offers a promising complementary
91 approach to reproducing historical reservoir operation processes. A range of data-driven ML
92 models, including artificial neural networks (ANN) (Özdoğan-Sarıkoç et al., 2023), nonlinear
93 autoregressive models with exogenous input (NARX) (Yang et al., 2019), and long short-term
94 memory networks (LSTM) (Tran et al., 2025), have been applied to simulate reservoir operations
95 using large-sample historical records. Among them, LSTM-based models have demonstrated
96 particularly favorable performance. Embedding physical mechanisms or operational constraints
97 can further enhance their ability to represent operational behaviors under hydrological extremes,
98 thereby allowing for a more accurate representation of high- and low-flow dynamics (Zheng et al.,
99 2022). Building on this line of research, coupling an LSTM-based reservoir operation module with
100 an LSTM-based hydrological process model can offer a pathway towards an integrated data-driven
101 framework for more automated drought diagnosis. This direction is motivated by key limitations
102 of traditional process-based hydrological models (e.g., VIC and CSSPV2), including their reliance
103 on basin- specific calibration and substantial requirements for physiographic inputs and
104 parameterization (e.g., topography, land use, and soil properties), which together constrain model
105 transferability across regions (Arsenault et al., 2023).

106 Beyond assessing how historical operating policies may shape future hydrological droughts,
107 it is also crucial to examine how effective optimal operating policies are in balancing operating
108 benefits against hydrological extremes. Optimal reservoir operation has been widely studied as a
109 way to enhance water-resource benefits without additional capital investment (He et al., 2025;
110 Wan et al., 2025). While some recent studies have incorporated drought-related performance

111 metrics (e.g., water-supply deficits or reliability) into operational analyses and optimization
112 frameworks (e.g., Huang et al. (2026)), these approaches primarily reflect the impacts of dry
113 conditions on water-supply performance rather than explicitly quantifying hydrological drought
114 states using drought indices. Consequently, the literature has largely focused on conceptual
115 analyses of the interplay between optimal reservoir operation and hydrological droughts, with
116 limited evidence from systematic implementation and evaluation in real-world water-management
117 practice(Huang et al., 2025; Ji et al., 2023). It therefore remains unclear whether embedding such
118 optimal strategies into existing management regimes would ultimately strengthen or weaken basin-
119 scale resilience to hydrological drought extremes under climate change.

120 Here, we aim to advance current reservoir-related drought assessment frameworks by (i)
121 replacing traditional process-based hydrological models with a fully data-driven LSTM framework
122 for hydrological drought quantification, and (ii) explicitly exploring the adaptive performance of
123 optimal operating policies under future climate change. Using the upper Hanjiang River basin in
124 China, a heavily reservoir-regulated system, as a representative case, we investigate the relative
125 and combined influences of climate change and reservoir operation on future hydrological
126 droughts under three CMIP6 shared socioeconomic pathways. Specifically, we first develop a
127 hybrid modelling framework that couples an LSTM-based hydrological model with a physics-
128 guided LSTM reservoir operation model to reproduce historical inflow and outflow, respectively.
129 The trained hybrid model is then driven by bias-corrected outputs from five CMIP6 GCMs to
130 project daily streamflow under near- and far-future scenarios. Hydrological drought characteristics,
131 including duration, frequency, and severity, are subsequently quantified using run theory for both
132 historical and future periods. Finally, we explicitly assess how adopting optimized operating
133 policies, in comparison with historical operating rules, may alter future hydrological drought

134 characteristics and basin-scale drought resilience, thereby revealing the potential trade-offs
135 between hydrological drought mitigation and operating benefits under a changing climate.

136

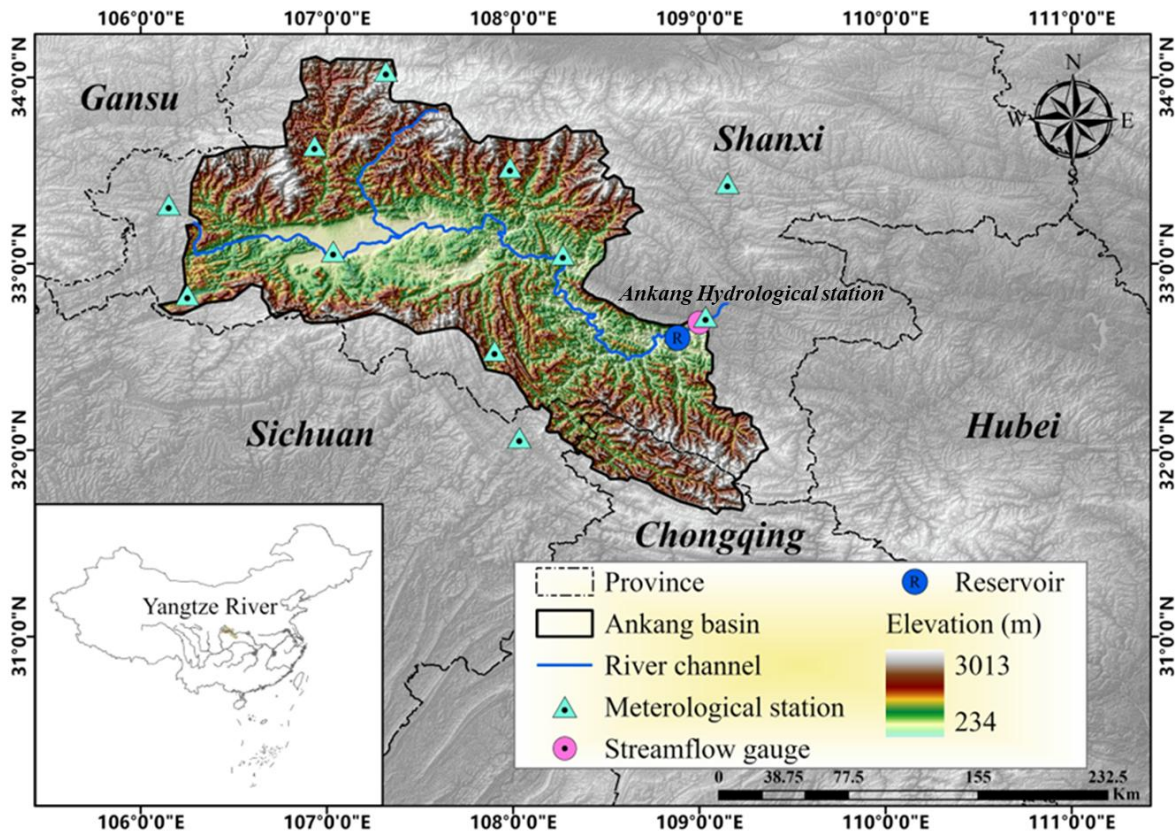
137 **2 Study Area and Data Description**

138 2.1 Study area

139 The Hanjiang River basin in central China plays a critical role in the regional water
140 economy of riparian provinces. As the longest tributary of the Yangtze River, the basin has
141 experienced extensive anthropogenic interventions, including the construction of a series of
142 reservoirs and inter-basin water transfer projects. In particular, the Ankang Reservoir, a large
143 reservoir situated near the outlet of the upper Hanjiang River basin (UHRB), exerts substantial
144 control on downstream discharge. Its operation primarily influences a ~30 km reach immediately
145 downstream (from the dam to the Ankang Hydrological Station), which we define as the regulated
146 reach in this study. As shown in Figure 1, the UHRB (31.0–34.5°N, 106.0–109.5°E) originates
147 from the southern foothills of the Qinling Mountains and terminates at the Ankang Hydrological
148 Station. The basin has a subtropical monsoon climate, with long-term mean annual precipitation,
149 temperature, and runoff depth of approximately 850mm, 15°C, and 500mm, respectively. The
150 flood season (May–October) contributes about 75% of annual precipitation, and streamflow
151 exhibits a broadly similar seasonal pattern, indicating a high sensitivity to both flood and drought
152 processes under the prevailing hydroclimatic regime (Jin et al., 2023).

153 With a total storage capacity of 3.2 billion m³, the Ankang Reservoir is the largest and most
154 downstream key control project within the UHRB. Commissioned in 1990, it is operated primarily
155 for hydropower generation (installed capacity: 850 MW), while also serving flood control and
156 navigation functions (Chinese National Committee on Large Dams, 2011). The reservoir controls

157 a natural catchment area of about 35,700 km² and has an active storage capacity of 1.47 billion m³.
158 To characterize inflow and outflow dynamics, we use discharge monitoring records collected at
159 the reservoir upstream inlet and at the Ankang Hydrological Station, which represent inflow to the
160 reservoir and regulated releases downstream, respectively.



161
162 **Figure 1.** Location of the upper Hanjiang River Basin (UHRB) and key hydrological elements,
163 showing the Ankang Reservoir and the downstream control section at the Ankang Hydrological
164 Station. The reservoir-regulated reach analysed in this study extends ~30 km downstream from the
165 dam to the station.

166
167 **2.2 Data**

168 The research datasets used in this study include both historical in-situ observations and
169 future climate projections. Historical meteorological records from eleven meteorological stations
170 (Figure 1) for the period 1992–2020 were obtained from the China Meteorological Administration

171 Data Sharing Service Center (CMA, <http://data.cma.cn>, last accessed on May 23, 2025), including
172 daily precipitation (Pr , mm), wind speed (Win , m/s), relative humidity (Rh , %), and air temperature
173 (maximum, minimum, and mean; Tem , °C). Basin-averaged precipitation and temperature time
174 series were derived using the Thiessen polygon method. Observed streamflow data for the same
175 historical period were obtained from the Bureau of Hydrology of the Yangtze Water Resources
176 Commission of China (<https://www.cjh.com.cn>, last accessed on May 23, 2025). The inflow to the
177 Ankang reservoir can be regarded as near-natural flow with negligible anthropogenic disturbance.

178 For future climate projections, a multi-model ensemble was adopted, consisting of five
179 GCMs under three Shared Socioeconomic Pathways (SSP126, SSP370, and SSP585), as listed in
180 Table 1. Several previous studies have shown that raw CMIP6 climate variables (e.g., precipitation,
181 air temperature) tend to be overestimated in Asia, with non-negligible uncertainties (Chai et al.,
182 2022). To reduce systematic biases in climate model outputs, bias-corrected daily data from the
183 Inter-sectoral Impact Model Intercomparison Project 3b (ISIMIP3b,
184 <https://data.isimip.org/search/tree/ISIMIP3b/InputData/>, last accessed on May 23, 2025) were
185 employed. These datasets were downscaled to a spatial resolution of $0.5^\circ \times 0.5^\circ$ using
186 observational climate data and cover the period 1850–2100. In the bias-adjustment procedure, a
187 trend-preserving parametric quantile mapping method was applied, accounting for
188 interdependencies among different climate variables, thereby providing significant improvements
189 over the previous ISIMIP2 framework (Lange, 2019). The robustness of ISIMIP3b has been
190 demonstrated across many regions of China (Kang et al., 2023; Yun et al., 2021a; He et al., 2023).
191 To assess climate change impacts, three equal 30-year periods were defined: the reference period
192 (1985–2014), the near-future period (2031–2060), and the far-future period (2071–2100).

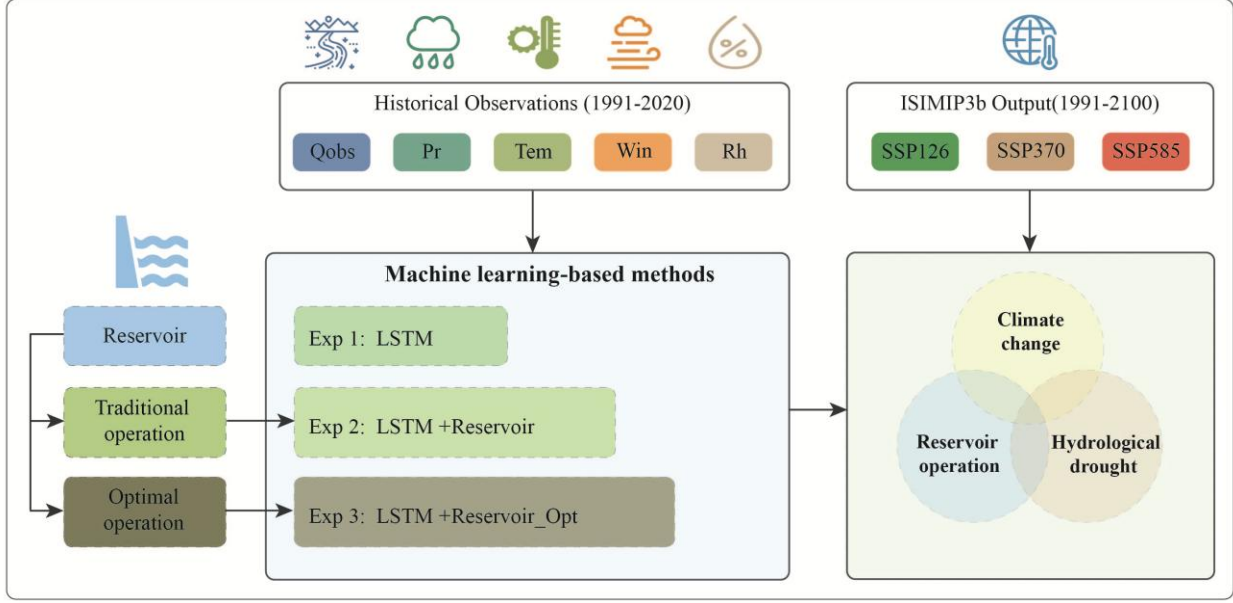
193
194 **Table 1.** Basic information on the five global climate models (GCMs) from ISIMIP3b

ID	Model	Modeling Center (or Group)	Institution Name	Horizontal resolution (lon. × lat.)
1	IPSL-CM6A-LR	IPSL	Institute Pierre Simon Laplace, France	2.50° × 1.27°
2	GFDL-ESM4	NOAA-GFDL	Geophysical Fluid Dynamics Laboratory, Princeton	1.25° × 1°
3	MPI-ESM1-2-HR	MPI-M	Max Planck Institute for Meteorology, Germany	0.9° × 0.9°
4	MRI-ESM2-0	MRI	Meteorological Research Institute, Japan	1.125° × 1.125°
5	UKESM1-0-LL	MOHC NERC	Met Office Hadley Centre and Natural Environment Research Council, UK	1.25° × 1.875°

195

196 **3 Methodology**

197 This section presents the methodology for exploring future hydrological droughts under
198 the coupled effects of climate change and reservoir operation, as illustrated in Figure 2. First, an
199 LSTM-based reservoir inflow simulation and a physics-based LSTM simulation for reservoir
200 operation are performed. Then, the ISIMIP3b outputs are used to drive the hybrid modeling
201 framework to project future streamflow scenarios and identify hydrological drought characteristics.
202 Finally, a series of numerical experiments are designed to investigate the individual roles of
203 climate change and reservoir operation in shaping future hydrological droughts. Each module is
204 described in detail in the following subsections.



205
 206 **Figure 2.** Schematic diagram of the modeling framework used to investigate the roles of climate
 207 change and reservoir operation in future hydrological droughts. The acronyms used in the
 208 experimental description panel are explained in Section 3.3.

209
 210 3.1 Long short-term memory (LSTM)

211 The LSTM is a variant of recurrent neural network that uses the backpropagation-through-
 212 time algorithm to address the vanishing gradient problem and retain information from earlier time
 213 steps (Hochreiter and Schmidhuber, 1997). It is specially structured with a gated memory block
 214 that introduces a memory cell and gating mechanisms compared with conventional neural
 215 networks (Hochreiter, 1998; He et al., 2022). The memory block (shown in Figure 3a) consists of
 216 a forget gate, an input gate, an output gate, and a memory cell. The forget gate determines which
 217 information from the previous cell state is discarded, whereas the input gate determines which
 218 information is used to update the cell state. The output gate then generates the hidden state based
 219 on the updated cell state. Mathematically, a typical memory block in an LSTM can be described
 220 by Equations (1) to (5).

221
$$f_t = \sigma(x_t W_f + h_{t-1} U_f + b_f) \tag{1}$$

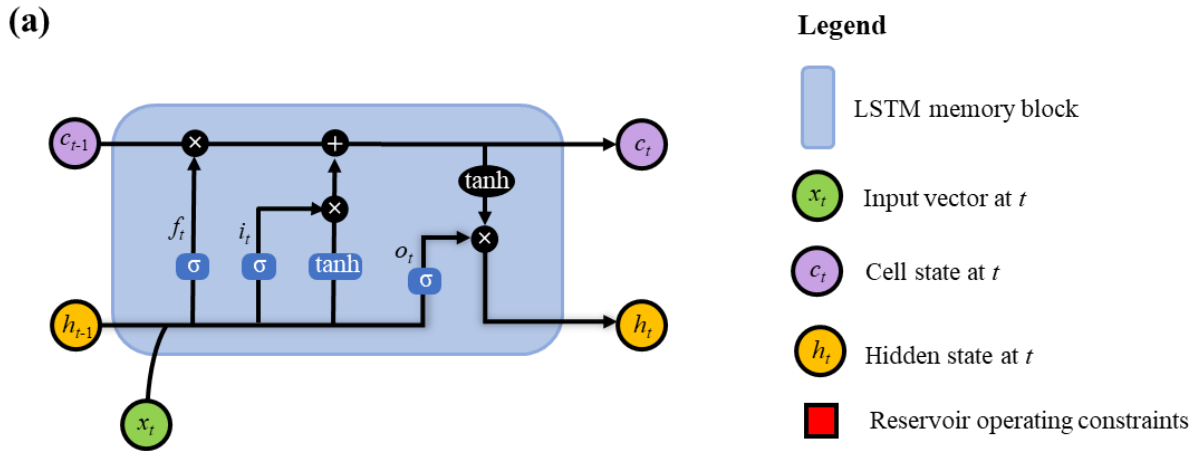
222
$$i_t = \sigma(x_t W_i + h_{t-1} U_i + b_i) \tag{2}$$

223
$$o_t = \sigma(x_t W_o + h_{t-1} U_o + b_o) \tag{3}$$

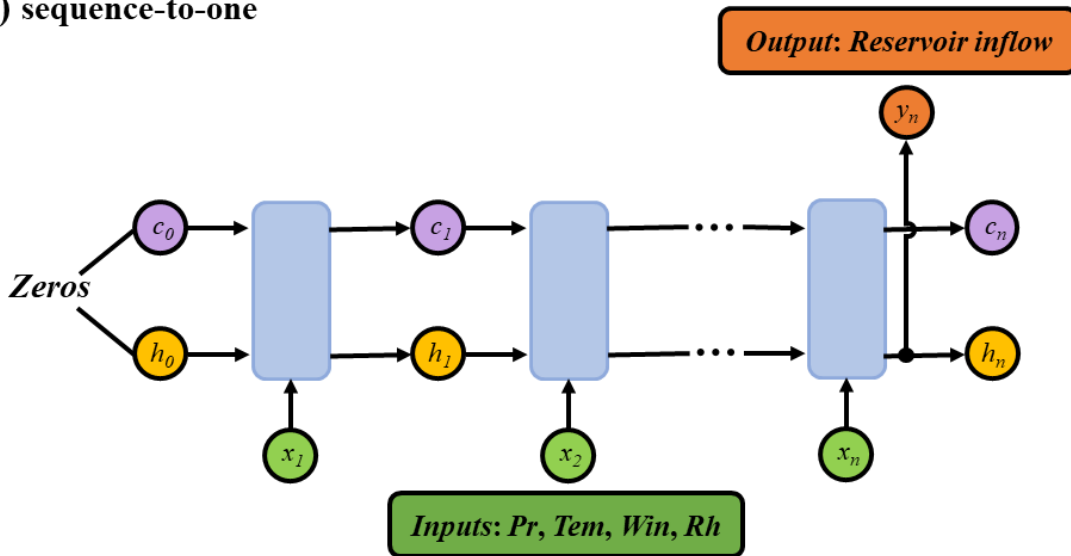
224
$$c_t = f_t \otimes c_{t-1} + i_t \otimes \tanh(x_t W_c + h_{t-1} U_c + b_c) \tag{4}$$

225
$$h_t = o_t \otimes \tanh(c_t) \tag{5}$$

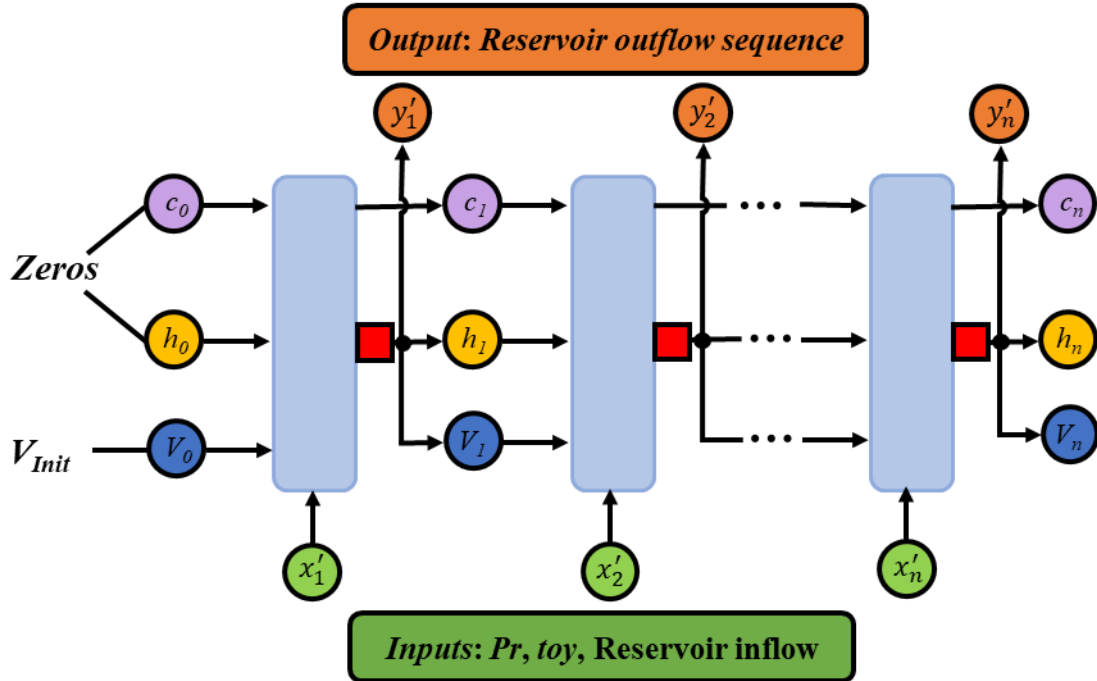
226 where x_t, f_t, i_t , and o_t denote the input variables, forget gate, input gate, and output gate at time t ,
 227 respectively. c_t and h_t represent the cell state and the hidden state at time t , while c_{t-1} and h_{t-1}
 228 are their values at the previous time $t-1$. W, U and b with various subscripts denote input weights,
 229 recurrent weights and bias terms, respectively. $\sigma(\cdot)$ is the sigmoid activation function with a return
 230 value ranging from 0 to 1. $\tanh(\cdot)$ is the hyperbolic tangent activation function with a return value
 231 ranging from -1 to 1. \otimes denotes element-wise multiplication.



(b) sequence-to-one



(c) sequence-to-sequence



232 **Figure 3.** Model structure of the long short-term memory (LSTM). (a) Internal structure of a
233 standard LSTM memory block, consisting of a forget gate, an input gate, an output gate, and a
234 memory cell. (b) A three-layer sequence-to-one LSTM architecture driven by correlated
235 meteorological inputs to simulate reservoir inflow. (c) A physics-guided LSTM-based sequence-
236 to-sequence model with antecedent reservoir storage, time of year (*toy*), precipitation and
237 simulated reservoir inflow as inputs to simulate reservoir release, where a red block following the
238 LSTM block represents a set of operational constraints, including the water balance equation and
239 reservoir storage and release limits.

240

241 3.1.1 LSTM-based reservoir inflow simulation

242 Some previous studies have shown that a three-layered LSTM with one hidden layer is
243 sufficiently robust to capture nonlinear rainfall-runoff relationships, although the black-box nature
244 of such models makes the interpretation of physical processes more challenging (Solanki et al.,
245 2025; Rehana and Rajesh, 2023; Liu et al., 2022). Following these studies, a sequence-to-one
246 LSTM architecture is adopted in this study to simulate near-natural reservoir inflow (Figure 3b).
247 The inputs to the LSTM consist of multiple meteorological variables, including precipitation, daily
248 maximum and minimum air temperature, relative humidity, and wind speed, with selected lag

249 times. The lag structure for each input variable is determined using cross-correlation analysis (Cui
250 et al., 2022) to account for delayed hydrological responses and catchment memory effects. The
251 model output is the near-natural reservoir inflow at time t . In addition to input selection, the number
252 of hidden units and the initial learning rate are treated as key hyperparameters of the LSTM model.
253 The hyperparameter tuning procedure is provided in detail in Table S1 of the Supporting
254 Information and is implemented using the Keras interface within the Python's TensorFlow
255 framework (Abadi et al., 2016).

256 Notably, antecedent reservoir inflow is not included as an input variable in the LSTM model,
257 although it is closely related to the target output in reality. This design choice is motivated by the
258 difficulty of accurately predicting antecedent inflow under future climate scenarios, where such
259 information can only be inferred from model simulations. Including antecedent inflow as an input
260 may therefore introduce additional uncertainty and lead to an artificial accumulation of simulation
261 errors. For historical simulations, meteorological data from 1992 to 2020 were used. The year 1992
262 was reserved as the model spin-up period to minimize the influence of initial conditions, while the
263 remaining data were divided into a calibration period (1993–2014) and a validation period (2015–
264 2020) to evaluate the out-of-sample performance of the trained LSTM model. Model calibration
265 was performed by maximizing the Nash–Sutcliffe efficiency (*NSE*; see Section 3.1.3 and
266 Equations (9)–(10)) using the Adam optimizer (Kingma and Ba, 2014). For future projections, the
267 period 1985–2100 was used to cover the full simulation span of the SSP scenarios. Within this
268 range, the period 1985–2014 was designated as the reference period, following ISIMIP3b protocol,
269 to evaluate future streamflow variations against a consistent historical baseline. The calibration
270 and validation periods are used exclusively for model training and evaluation, whereas the
271 reference period is treated independently for climate impact assessment.

272 3.1.2 Derivation of historical operation patterns with a physics-guided LSTM model

273 For human-intervened reservoir operation, which often involves substantial expert knowledge,
274 LSTM, as a state-of-the-art machine learning technique, has been shown to outperform traditional
275 empirical approaches in learning operating rules from large historical records (Zheng et al., 2022;
276 Longyang and Zeng, 2023; García-Feal et al., 2022). In contrast to the inflow simulation in Figure
277 3(b), we constructed a three-layer sequence-to-sequence LSTM model (Figure 3(c)) to simulate
278 reservoir release.

279 Following the guidelines of the local reservoir management agency, antecedent reservoir
280 storage, time of year, precipitation, and reservoir inflow were used as the major inputs. To improve
281 the robustness of the model for future simulations, we used the LSTM-simulated inflow from
282 Section 3.1.1 rather than observed inflow records. In addition, a state variable representing
283 reservoir storage was incorporated and initialized at the flood-limited water level, which can be
284 updated via the state transition equation (i.e., the water balance equation in Equation (6)). To avoid
285 physically unrealistic states during the simulation (e.g., violation of operational constraints),
286 additional operational constraints, including reservoir storage limits in Equation (7) and reservoir
287 release limits in Equation (8), were also incorporated, resulting in a physics-guided LSTM model.

$$288 \quad V_{t+1} = V_t + (I_t - O_t) \cdot \Delta t \quad (6)$$

$$289 \quad V_{min} \leq V_t \leq V_{max} \quad (7)$$

$$290 \quad O_{min} \leq O_t \leq O_{max} \quad (8)$$

291 where V_t and V_{t+1} are the reservoir storage (m^3) at the beginning and end of time step t ,
292 respectively; I_t and O_t are the reservoir inflow (m^3/s) and release (m^3/s) at time t , respectively;
293 V_{min} and V_{max} are the allowable minimum and maximum reservoir storage (m^3), respectively;
294 O_{min} and O_{max} are the allowable minimum and maximum reservoir release (m^3/s), respectively;
295 and Δt is the simulation time step (s).

296

297 3.1.3 Objective function for model calibration

298 To simultaneously improve the simulations of near-natural reservoir inflow and human-

299 regulated release, the average NSE (NSE_{ave}) was defined as the optimization objective.

$$300 \quad \max NSE_{ave} = 1/2 \times (NSE_{inflow} + NSE_{release}) \quad (9)$$

301 where NSE_{inflow} and $NSE_{release}$ denote the NSE values for the simulated inflow and release,

302 respectively. For a given time series, NSE is computed as

$$303 \quad NSE = 1 - \frac{\sum_{t=1}^T (Q_t^{sim} - Q_t^{obs})^2}{\sum_{t=1}^T (Q_t^{obs} - \overline{Q^{obs}})^2} \quad (10)$$

304 where Q_t^{sim} and Q_t^{obs} denote the simulated and observed streamflow at time t , respectively; $\overline{Q^{obs}}$

305 is the mean observed streamflow over the evaluation period; and T is the total number of time steps.

306 NSE ranges from $-\infty$ to 1, with 1 indicating a perfect match between simulated and observed

307 streamflow.

308 3.2 Standard streamflow index

309 This study used the standardized streamflow index (SSI) to characterize hydrological

310 drought, because it only requires streamflow data and has been widely applied across a range of

311 timescales, including 1-, 3-, 12-, and 24-month periods (Vicente-Serrano et al., 2012; Smith et al.,

312 2019; Gu et al., 2020; Shukla and Wood, 2008). The 1-month (SSI-1) and 3-month (SSI-3) indices

313 represent short-term hydrological conditions, whereas longer aggregation windows such as SSI-

314 12 and SSI-24 reflect persistent, long-term hydrological drought conditions. Here, SSI-1, SSI-3,

315 and SSI-12 were selected to represent monthly, seasonal, and annual hydrological drought,

316 respectively.

317 In the calculation of SSI for each calendar month m ($m = 1, 2, \dots, 12$) at a specific time

318 scale, a Pearson type-III distribution was fitted to the corresponding aggregated streamflow series

319 (Q) during the reference period. The goodness-of-fit was evaluated using the Kolmogorov–
320 Smirnov test. The cumulative distribution function is expressed as:

$$321 \quad F_m(Q) = \frac{\beta^\alpha}{\Gamma(\alpha)} \int_x^\infty (Q - \omega)^{\alpha-1} e^{-\beta(Q-\omega)} dr \quad (11)$$

322 where $F_m(Q)$ is the cumulative distribution function; α , β , and ω are the shape, scale, and location
323 parameters of the distribution, respectively, which were estimated using the L -moment method
324 (Hosking, 1990). The SSI values were then obtained by applying the standard normal transforming
325 process (Φ^{-1}).

$$326 \quad SSI = \Phi^{-1}(F_m) \quad (12)$$

327 To ensure consistency in comparing hydrological drought characteristics between
328 historical and future periods, the distribution parameters estimated from the 30-year reference
329 period (1985–2014) were applied to the two future 30-year periods (i.e., the near-future and far-
330 future) when computing SSI, following common practice in climate impact assessment studies
331 (Yun et al., 2021b; Wan et al., 2018).

332 The characteristics (e.g., duration, severity, and intensity) of hydrological drought episodes
333 were extracted using run theory (Yevjevich, 1967). A drought episode begins when SSI falls below
334 a specific threshold (-0.5) and ends when SSI rises above the threshold, as illustrated by the two
335 drought episodes D_0 and D_1 in Figure 4. Drought duration is defined as the length of the drought
336 episode, while drought severity is defined as the cumulative deficit of SSI values below the drought
337 threshold during the episode. Drought intensity is defined as the average deficit below the
338 threshold, calculated as severity divided by duration. In particular, two adjacent drought branches
339 (d_0 and d_2) can be merged into a single drought episode (i.e., the third drought episode in Figure
340 4) when the inter-event time d_1 is no longer than the time evaluation criterion t_c ($t_c = 2$ months in
341 this study) and SSI remains below the allowable upper threshold during this interval (Zhou et al.,

2021; Wu et al., 2017). Under this condition, the merged drought duration is calculated as $D_2 = d_0 + d_1 + d_2$ and the severity is $S_2 = s_0 + s_2$. Since drought intensity is defined as the ratio of severity to duration, only two drought characteristics, duration (D) and severity (S), are used in this study to comprehensively describe each drought episode.

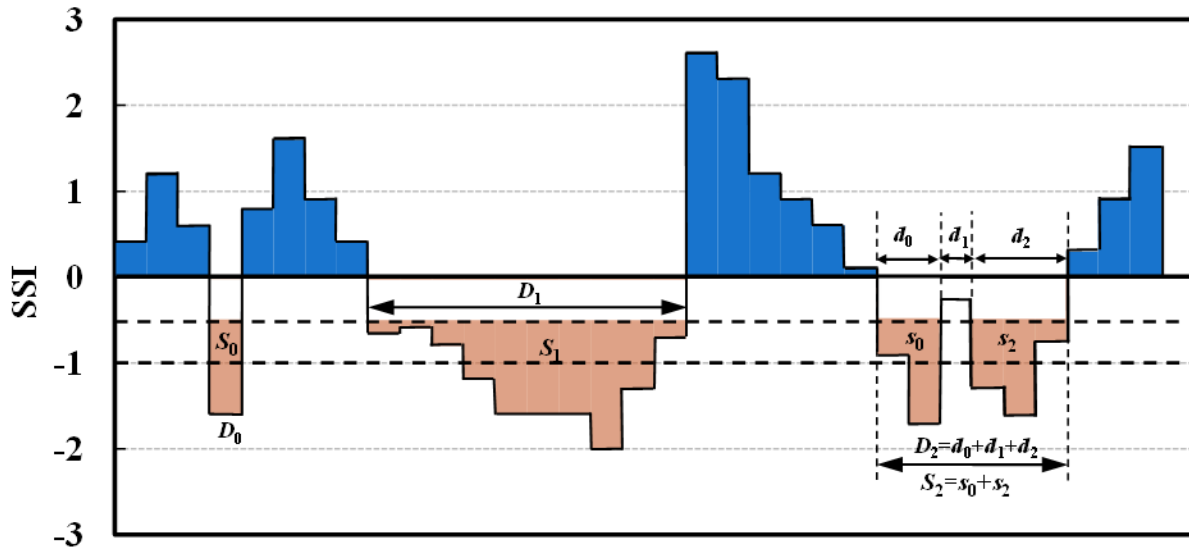


Figure 4. Identification of hydrological drought events and characteristics using run theory. Three types of drought episodes are illustrated in orange: episode D_0 with severity S_0 , episode D_1 with severity S_1 , and a merged episode D_2 with severity S_2 , where $D_2 = d_0 + d_1 + d_2$ and $S_2 = s_0 + s_2$. The two adjacent drought branches d_0 and d_2 are merged when the interval d_1 is no longer than the time evaluation criterion t_c ($t_c = 2$ months in this study) and the SSI remains below the allowable upper threshold during d_1 .

3.3 Experimental Design

To systematically explore the roles of climate change and reservoir operation in shaping future hydrological droughts, a set of numerical experiments were designed (Table 2). Specifically, OBS/LSTM and OBS/LSTM+Reservoir denote simulations driven by observed CMA meteorological forcing, without and with reservoir operation, respectively. Similarly, ISIMIP3b_ref/LSTM and ISIMIP3b_ref+Reservoir represent simulations driven by ISIMIP3b forcing during the reference period, without and with reservoir operation, respectively. The

361 experiments ISIMIP3b_fut/LSTM and ISIMIP3b_fut/LSTM+Reservoir further incorporate future
 362 climate forcing to quantify the progressive impacts of climate change and reservoir operation on
 363 future projections. Notably, the term “Reservoir” in these experiments refers to the historical
 364 reservoir operation policy over 1992–2020, which was derived from the physics-guided LSTM
 365 model.

366 There is little focus on the evolution of trade-offs between operating benefits and drought
 367 risks, although a large body of literature points out the necessity of optimizing reservoir operation
 368 policies (Ji et al., 2023; Brunner, 2021; Wu et al., 2022; Firoz et al., 2018). To this end, a classical
 369 multi-objective decision-making optimization was implemented for the Ankang Reservoir to
 370 maximize both hydropower generation and the power generation guarantee rate. The optimal set
 371 of alternative operating policies π_{θ}^* under historical climate conditions w^H was obtained by solving
 372 the following problem.

$$373 \quad \pi_{\theta}^* = \underset{\pi_{\theta}}{\operatorname{arg\,max}} f(\pi_{\theta}, w^H) = |f_{THP}(\pi_{\theta}, w^H), f_{PGR}(\pi_{\theta}, w^H)| \quad (13)$$

374 where f is the objective vector consisting of $[f_{THP}, f_{PGR}]$ (see Text S2 for details). The operating
 375 policies π_{θ} was parameterized using Gaussian radial basis functions, which have been shown to
 376 be effective for reservoir operation optimization (Quinn et al., 2019; Bertoni et al., 2019). The
 377 optimization was performed using the Non-dominated Sorting Genetic Algorithm II (NSGA-II;
 378 (Deb et al., 2002). The resulting Pareto-optimal policies, π_{θ}^* , were then applied under future
 379 climate scenarios to investigate the potential co-benefits and trade-offs between hydropower
 380 generation and drought risk reduction. This exploratory analysis corresponds to the
 381 ISIMIP3b_fut/LSTM+Reservoir_Opt experiment in Table 2, and detailed results are presented in
 382 Section 4.4.

383 **Table 2.** Experimental design and scenario configurations used in this study.

Experiment	Meteorological forcing	Simulation period	Climate change	Traditional reservoir operation	Optimal reservoir operation
OBS/LSTM	Observations	1992–2020	–	–	–
OBS/LSTM + Reservoir	Observations	1992–2020	–	✓	–
ISIMIP3b_ref/LSTM	ISIMIP3b reference	1985–2014	–	–	–
ISIMIP3b_ref/LSTM+Reservoir	ISIMIP3b reference	1985–2014	–	✓	–
ISIMIP3b_fut/LSTM	ISIMIP3b future	2031–2060, 2071–2100	✓	–	–
ISIMIP3b_fut/LSTM+Reservoir	ISIMIP3b future	2031–2060, 2071–2100	✓	✓	–
ISIMIP3b_fut/LSTM+Reservoir_Opt	ISIMIP3b future	2031–2060, 2071–2100	✓	–	✓

384

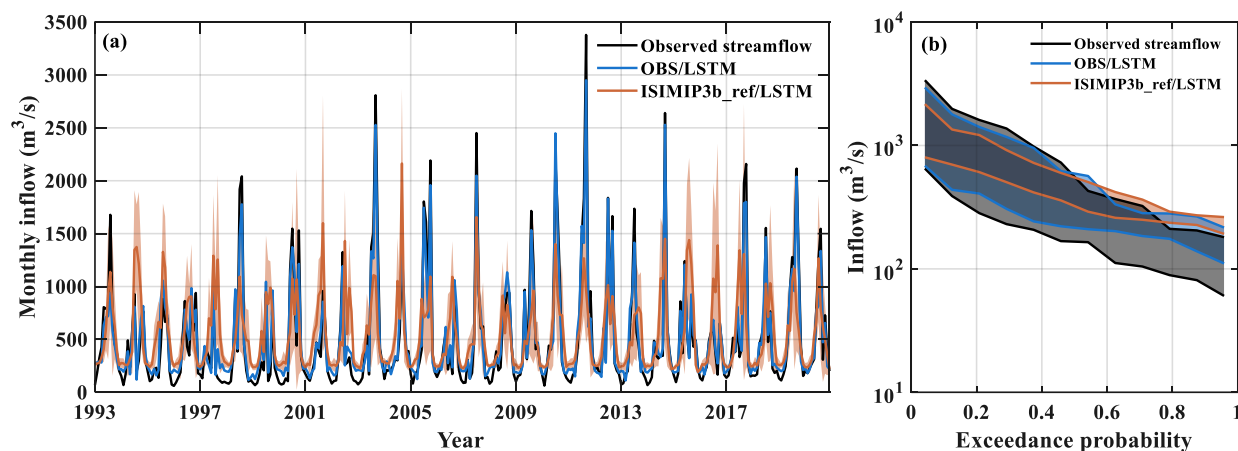
385 4 Results and Discussion

386 4.1 Model calibration and validation

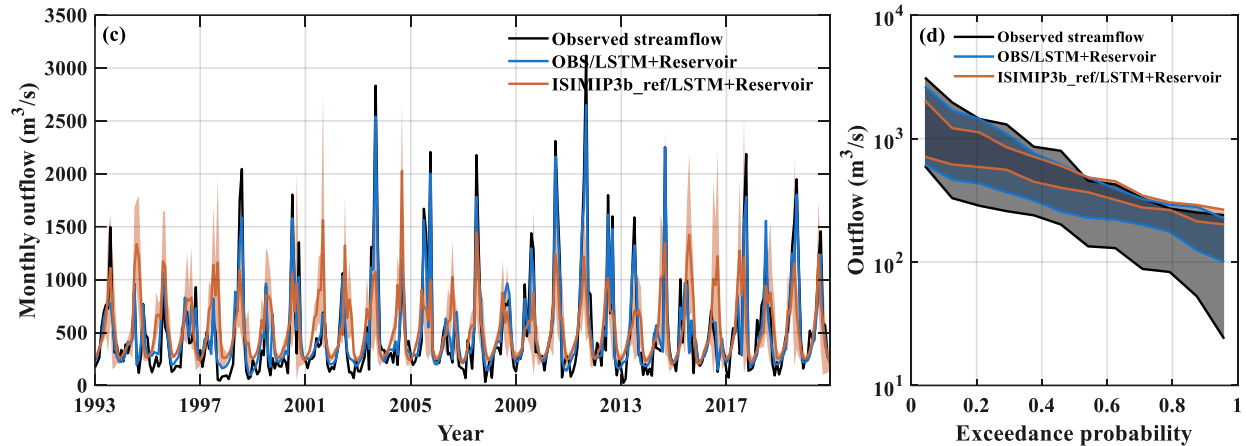
387 Figure 5 presents the calibration and validation results for both reservoir inflow and release
388 using the LSTM-based modeling framework. As shown in Figure 5(a), the LSTM model
389 reproduced the near-natural reservoir inflow well at the monthly scale, with *NSE* values of 0.95
390 and 0.93 for the calibration and validation periods, respectively. Figure 5(b) further evaluates the
391 model performance across the full flow regime using flow duration curves (FDCs), showing that
392 the simulated flow distribution generally follows the observed pattern across a wide range of
393 exceedance probabilities. Figure 5(c) illustrates the comparison between observed and simulated
394 reservoir release at the Ankang hydrological station. The seasonal shift between observed inflow
395 and release curves (black lines in Figure 5(a) and 5(c)) suggests that reservoir operations have
396 reshaped streamflow seasonality, with an estimated 5–21% of downstream flow withheld by the
397 Ankang reservoir during June–October and released later in the year. This operational pattern is

398 well captured by the LSTM+Reservoir model driven by observed meteorological forcings,
399 yielding *NSE* values of 0.91 and 0.89 for the calibration and validation periods, respectively. While
400 slightly lower than those for inflow, these values reflect satisfactory performance given the
401 complexity of human-influenced reservoir operations.

402 Figures 5(a) and 5(c) also show the ensemble-averaged hydrographs from the
403 ISIMIP3b_ref/LSTM and ISIMIP3b_ref/LSTM+Reservoir experiments, driven by ISIMIP3b
404 meteorological forcings rather than historical meteorological observations. The model
405 performance under these forcings is noticeably weaker than that of the OBS/LSTM and
406 OBS/LSTM+Reservoir configurations, likely due to limitations of ISIMIP3b in characterizing
407 regional-scale meteorological regimes (Kang et al., 2023). FDCs in Figure 5(b) and 5(d) further
408 indicate that simulated low flows tend to be overestimated at high exceedance probabilities, which
409 may affect the absolute magnitude of simulated low-flow conditions. Nevertheless, since our
410 subsequent analyses focus on changes relative to the ISIMIP3b_ref baseline, the influence of this
411 systematic bias is likely to be reduced; therefore, the simulations are used for the subsequent
412 hydrological drought analysis.



413



414

415 **Figure 5.** Evaluation of monthly reservoir inflow and release simulations. (a, c) Hydrographs of
 416 reservoir inflow and release; (b, d) Corresponding flow duration curves (FDCs). Simulations
 417 driven by meteorological observations (OBS/LSTM and OBS/LSTM+Reservoir) are marked as
 418 blue lines, while simulations driven by ISIMIP3b_ref forcings (ISIMIP3b_ref/LSTM and
 419 ISIMIP3b_ref/LSTM+Reservoir) are marked as orange lines. Shaded bands in (a, c) indicate the
 420 ensemble mean ± 1 standard deviation of simulations driven by ISIMIP3b GCM forcings, while
 421 those in (b, d) denote the interannual range (min–max envelope) of annual FDCs.

422

423 Changes in reservoir storage (ΔS) represent another key variable in our operation simulations

424 and are also used in the hydropower performance assessment in Section 4.4. Figure 6 illustrates

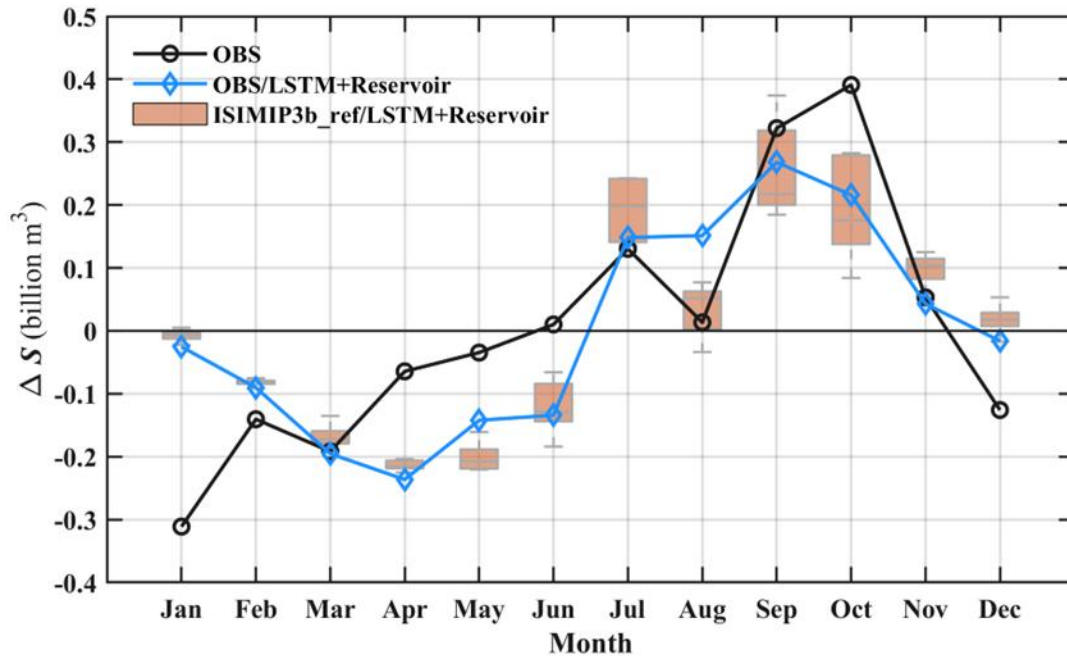
425 the observed and simulated mean monthly storage variations over the available period 2001–2010.

426 Both the OBS/LSTM+Reservoir and ISIMIP3b_ref/LSTM+Reservoir simulations reproduce the

427 observed dynamics well, particularly the storage accumulation from July to November. With

428 correlation coefficients between simulated and observed storage series ranging from 0.70 to 0.73,

429 the model provides a reasonable approximation of reservoir operations.



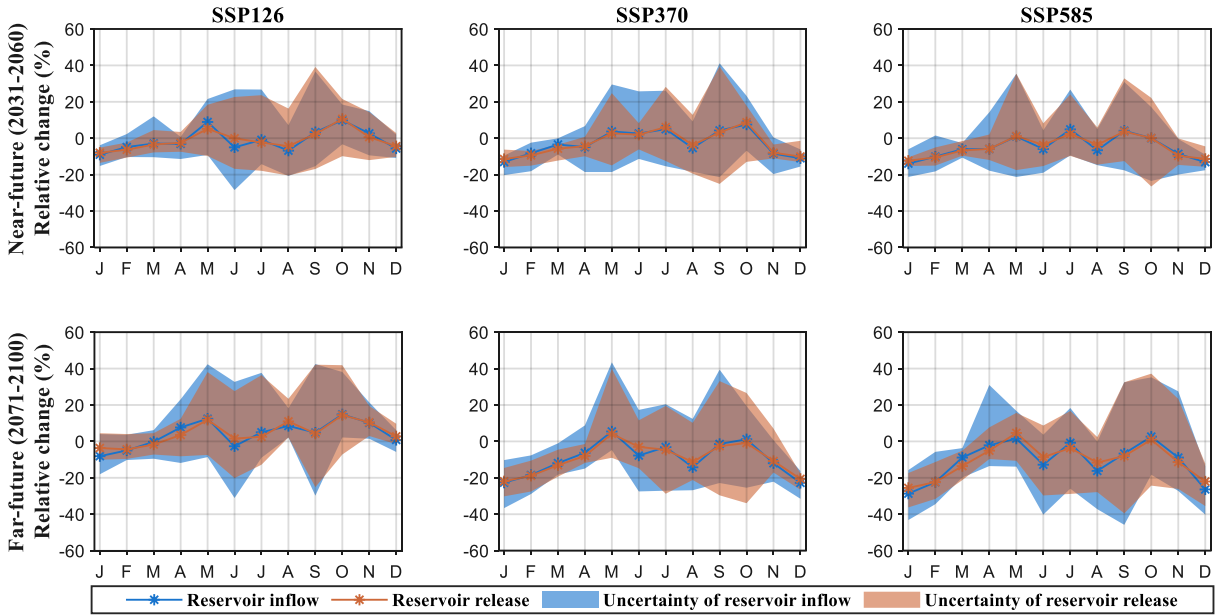
430
 431 **Figure 6.** mean monthly storage variations (ΔS) in the Ankang reservoir during 2001-2010. The
 432 black dotted line represents the multi-year observations. The blue line shows the
 433 OBS/LSTM+Reservoir simulation. The orange boxplots represent the
 434 ISIMIP3b_ref/LSTM+Reservoir ensemble simulations driven by five ISIMIP3b GCMs.

435
 436 **4.2 Streamflow variation under the impacts of climate change and reservoir operation**

437 Climate change scenarios in ISIMIP3b project a consistent upward trend in both
 438 precipitation and temperature over the UHRB during the future periods, relative to the reference
 439 period (at a significance level of $p < 0.05$ based on the Mann-Kendall test). Among the SSP
 440 scenarios, SSP126 presents an increase in precipitation (+7.3% to +13.3%) and a modest
 441 temperature rise (+1.7°C to +1.9°C). SSP370 shows a similar increase in precipitation (+7.3% to
 442 +11.2%) but a more pronounced warming (+1.8°C to +4.0°C). Under SSP585, the largest increases
 443 are projected for both precipitation (+8.0% to +15.8%) and temperature (+2.3°C to +5.3°C). As a
 444 result of the combined climatic drivers, the multi-year average reservoir inflow is expected to
 445 increase from +0.3% (near-future, 2031–2060) to +5.5% (far-future, 2071–2100) under SSP126.
 446 Under SSP370 and SSP585, it is expected to shift from +0.2% (near-future) to -7.0% (far-future),

447 and from -2.6% (near-future) to -8.4% (far-future), respectively, suggesting a potential long-term
448 decline despite short-term gains. This implies that warming-induced evaporation losses may
449 outweigh the compensating effects of increased precipitation, especially under higher-emission
450 scenarios (Sato et al., 2022).

451 Figure 7 further illustrates the projected relative change in monthly mean streamflow
452 across future periods and SSP scenarios, explicitly highlighting the seasonal influence of both
453 climate change and reservoir operation. Substantial inter-model uncertainty is evident, particularly
454 under SSP585 during the far-future flood season, where streamflow changes range from -45% to
455 $+43\%$. Despite this variability, the ensemble mean reveals a consistent signal: positive deviations
456 are mainly concentrated in the flood season, while most other months are expected to experience
457 declining streamflow. This asymmetric seasonal response suggests an intensification of
458 hydrological seasonality, with wetter periods becoming more flood-prone and drier periods
459 experiencing heightened water stress. In general, human-regulated reservoir operation has the
460 potential to moderate the magnitude of future monthly streamflow changes. However, across all
461 scenarios, the extent to which the Ankang Reservoir alters streamflow patterns remains rather
462 limited, which may be attributable to its primary operational objective of hydropower generation,
463 with relatively little emphasis on shaping the flow regime itself. Further investigation into effective
464 reservoir management is warranted.



465

466 **Figure 7.** Relative changes in projected monthly reservoir inflow and release for two future periods
 467 and three SSP scenarios, relative to the reference period 1985–2014. Lines are the ensemble mean
 468 of the five GCMs, and shaded areas represent the uncertainty across the five GCMs.

469

470 4.3 Changes in hydrological drought events

471

472

473

474

475

476

477

478

479

480

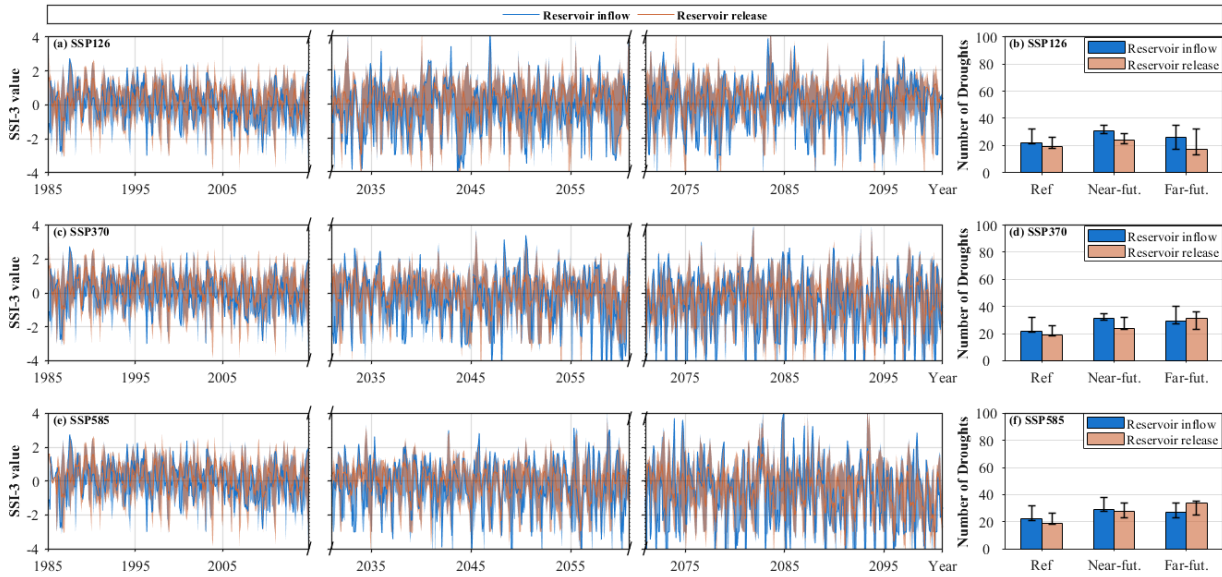
481

To comprehensively evaluate future hydrological droughts, we analyzed both the continuous SSI-based drought characteristics and the annual drought event frequency and severity under different climate and reservoir operation scenarios. The time series of SSI-3 associated with reservoir inflow and release, together with their ensemble spreads under three emission scenarios, are shown in Figure 8, with the SSI-1 and SSI-12 results provided in Figures S1 and S2, respectively. SSI-1 and SSI-3 exhibit stronger short-term fluctuations within $[-3, 3]$, whereas SSI-12 shows smoother variability, reflecting more stable long-term dynamics. Consistent with the projected decreases in streamflow, all three indices (SSI-1, SSI-3, and SSI-12) show a slight worsening trend over time, particularly under SSP370 and SSP585, indicating an increased likelihood of drought occurrence in the future (Figures 8(b), 8(d) and 8(f)). We therefore quantified the number of drought events for three periods estimated by the GCMs and summarized them on

482 the right side of Figures 8, S1 and S2. The Results suggest that drought occurrence is generally
483 higher in the future periods than in the reference period, despite substantial inter-model
484 discrepancies across GCMs. The near-future period shows slightly more drought events than the
485 far-future period, with more small and frequent droughts. In addition, as shown in Figure 8 (b),
486 (d), and (f), reservoir operation can mitigate the frequency of drought in the reference period but
487 does not completely remove the risk of hydrological drought under future climate change.
488 Reservoir operation is better at preventing short-term droughts, as the drop in the number of
489 droughts associated with reservoir release versus inflow is significant for SSI-1 in Figure S1 but
490 not for SSI-12 in Figure S2. It may be related to the limited annual regulation capacity of the
491 Ankang reservoir.

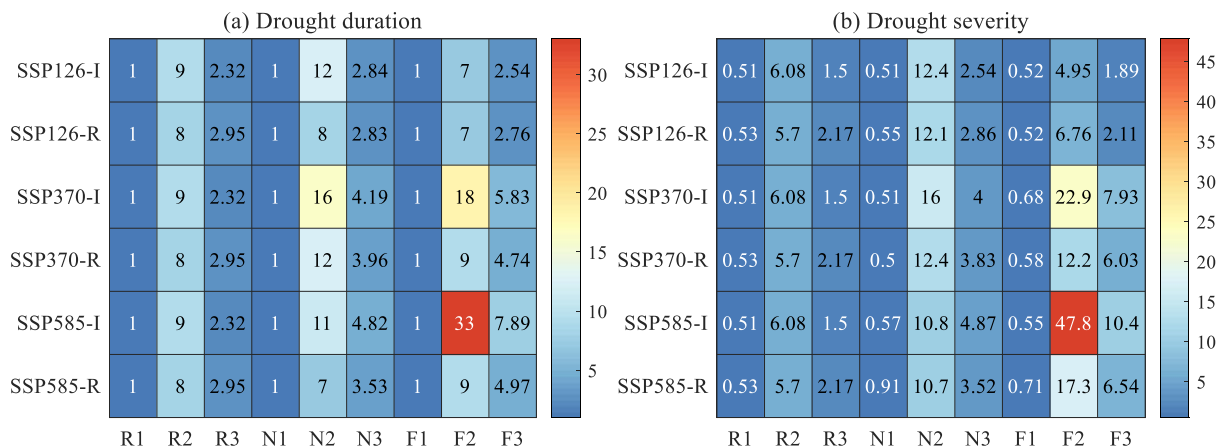
492 A more comprehensive assessment of SSI-3 drought characteristics, including duration and
493 severity, is provided in Figure 9 (see Figure S3 and Figure S4 for SSI-1 and SSI-12, respectively).
494 Both drought duration and severity are projected to deteriorate under future climate change. The
495 most extreme SSI-3 drought event is projected to occur in the far-future period under SSP585,
496 with a maximum duration of 33 months and a maximum severity of 47.8. It is followed by SSP370,
497 with an 18-month duration and a severity of 22.9, and finally SSP126, with a 12-month duration
498 and a severity of 12.4. The drought duration and severity associated with SSI-1 and SSI-12 show
499 a similar pattern. Overall, SSP585 exerts the most pronounced impact on hydrological drought in
500 the region. Notably, reservoir operation provides substantial relief from extreme hydrological
501 drought by redistributing more short-term drought events through impoundment and release
502 regulation. For the far-future period under SSP585, the maximum duration associated with SSI-3
503 is reduced by 72.73% and the maximum severity is reduced by 63.81% due to reservoir operation.
504 The original extreme hydrological drought associated with SSI-1 can likewise be regulated to a

505 modest level (Figure S3). It is yet less evident for SSI-12, which requires additional human
 506 interventions to improve.



507 **Figure 8.** Hydrological drought SSI-3 for reference and future periods over the UHRB. (a) Time
 508 series of SSI-3 associated with reservoir inflow and release for the low-emission SSP126 scenario.
 509 Blue and orange intervals indicate their uncertainties, respectively. (b) Number of drought events
 510 for the reference period (1985–2014), near-future period (2031–2060), and far-future period
 511 (2071–2100). Colored bars are ensemble means and error bars represent the estimated difference
 512 in the number of drought events among the five GCMs. (c-d) is the same as (a-b), but for the
 513 medium-emission SSP370 scenario. (e-f) is the same as (a-b), but for the high-emission SSP585
 514 scenario.
 515

516



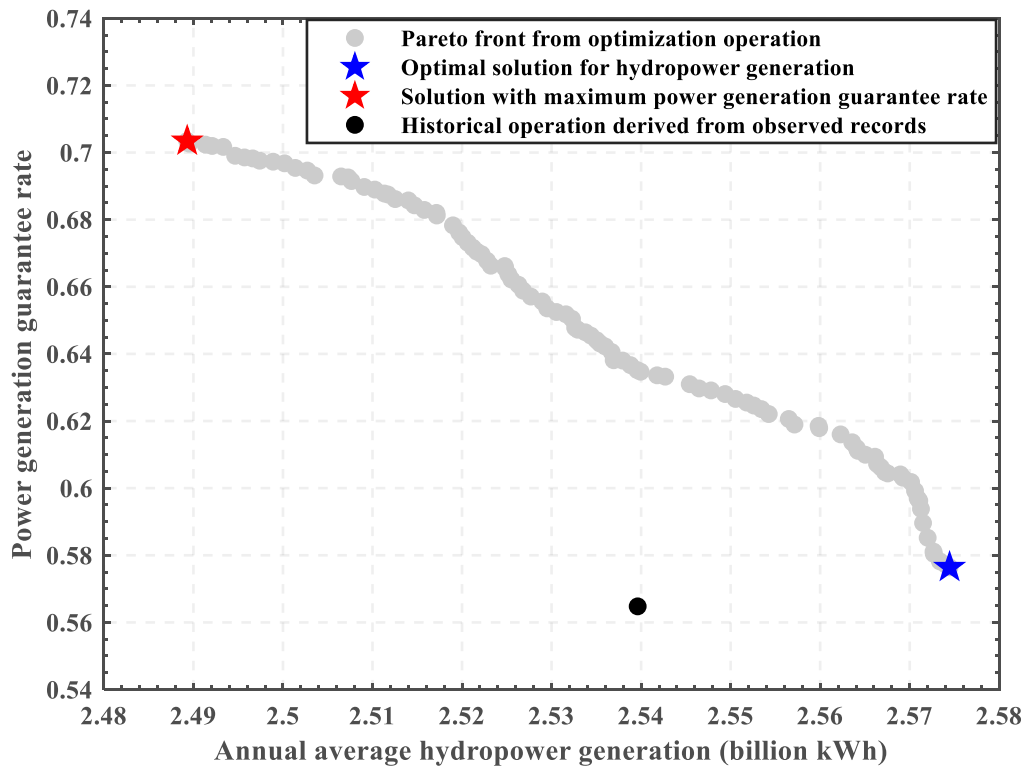
517 **Figure 9.** Heat map representation of (a) drought duration and (b) drought severity for the GCM-
 518 averaged SSI-3 series. The symbols R1, R2 and R3 indicate the minimum, maximum, and mean
 519 values during the reference period (1985–2014). N1, N2 and N3 are the same, but for the near-
 520

521 future period (2031–2060). F1, F2, and F3 are for the far-future period (2071–2100). Additionally,
522 SSP126-I and SSP126-R are associated with reservoir inflow and release in the SSP126 scenario,
523 SSP370-I and SSP370-R with the SSP370 scenario, and SSP585-I and SSP585-R with the SSP585
524 scenario.

525

526 4.4 Adaptability of optimal operating policies to future hydrological droughts

527 Optimal reservoir operating policies can serve as a potential adaptation measure to future
528 climate change. Previous studies have highlighted their potential in mitigating the adverse impacts
529 of severe hydrological events (Wu et al., 2023; Sun et al., 2023; Yun et al., 2021b; Levey and
530 Sankarasubramanian, 2025). However, practical validation remains limited. In this section, we
531 applied the NSGA-II algorithm to derive 100 Pareto-optimal operating policies using historical
532 inflow observations (Figure 10), and examined their implications for future hydropower generation
533 and drought characteristics under climate change.



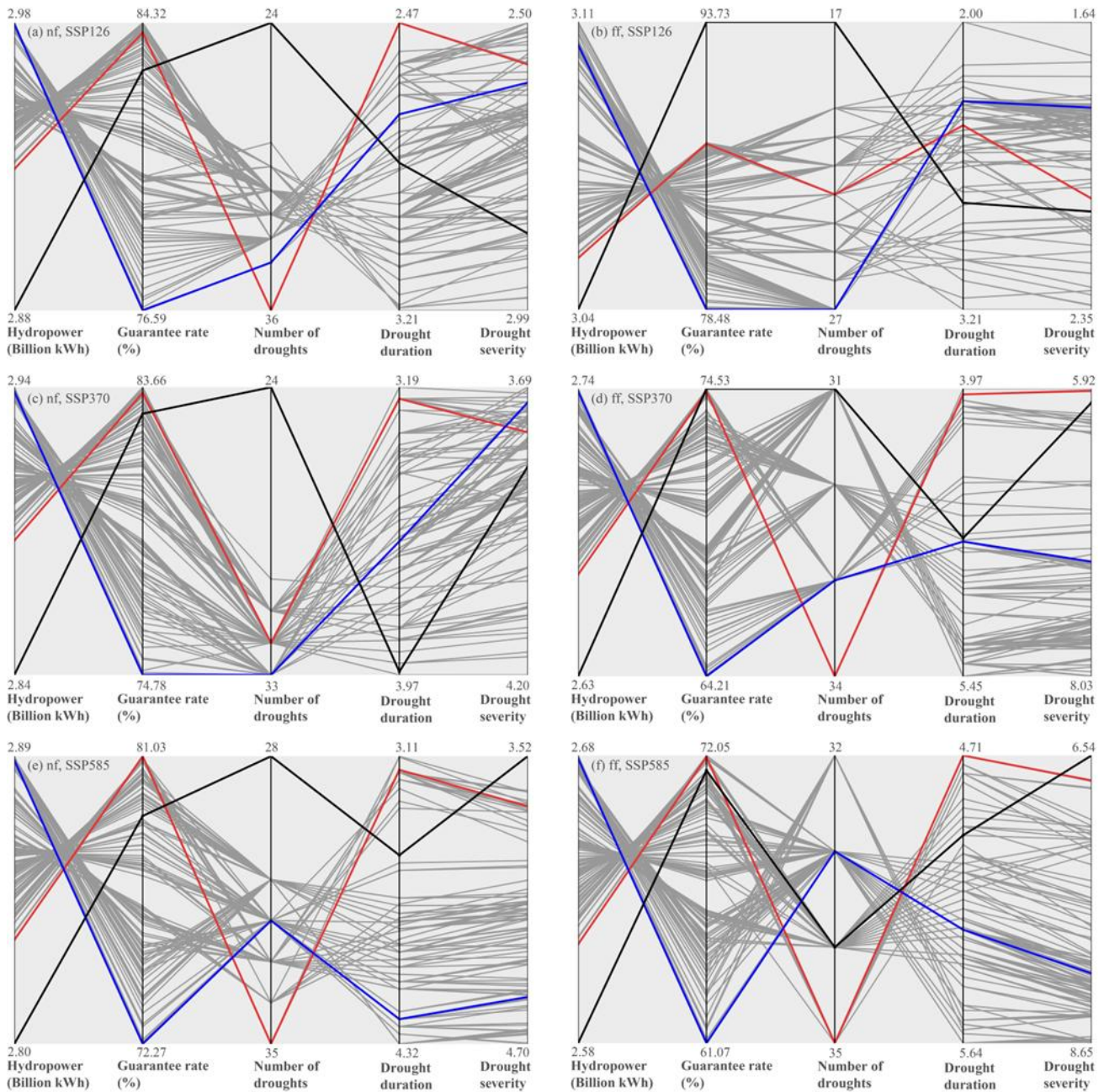
534

535 **Figure 10.** Trade-off between annual average hydropower generation and power generation
536 guarantee rate for the Ankang Reservoir. Each grey dot represents an optimal operating policy

537 identified using the NSGA-II algorithm, forming the Pareto front. The blue star marks the solution
538 with the maximum hydropower generation, while the red star indicates the solution with the
539 highest power generation guarantee rate. The black dot represents the historical operation derived
540 from observed records.
541

542 The simulation results of these 100 optimal operating policies for hydropower generation
543 and SSI-3 drought characteristics under future climate change conditions are reported in Figure 11
544 using parallel coordinate plots. The historically derived operating policy is outlined in black for
545 comparison. These plots show each operating policy as a grey line that intersects each vertical axis
546 at the achievable performance value, and the axes are oriented with the optimal direction upwards.
547 The ideal policy in Figure 11 is, therefore, a horizontal line across the top of each axis.
548 Nevertheless, these lines usually intersect between adjacent axes because superior performance in
549 one indicator comes at the cost of poorer performance in another. For instance, lower power
550 generation guarantee rates inevitably constrain the goal of maximizing annual average hydropower
551 generation. All optimal policies have similar future annual average hydropower generation, except
552 for the far-future period under SSP126. They have a wide range of guarantee rates, such as
553 76.59%–84.32% for the near-future period under SSP126 and 61.07%–72.05% for the far-future
554 period under SSP585. Additionally, as can be seen in all subplots of Figure 11, all the optimal
555 operating policies result in higher hydropower generation but also a higher drought frequency than
556 the historically derived policy. The SSI-3 series associated with optimal reservoir release is broken
557 into more drought events where the average duration and severity of droughts do not change
558 substantially. The most challenging drought management task remains in the future-period under
559 SSP585, during which the historically derived policy has the lowest drought severity. On the whole,
560 a small number of optimal policies can achieve robust and satisfactory performance of all

561 considered indicators across plausible future scenarios, demonstrating their potential for mitigating
 562 short-term hydrological droughts.



563 **Figure 11.** Trade-offs among hydropower generation, guarantee rate, and SSI-3 drought
 564 characteristics under optimal and historical reservoir operating policies using parallel coordinates
 565 plots. Panels (a–b) correspond to the near-future (nf) and far-future (ff) under SSP126, (c–d) under
 566 SSP370, and (e–f) under SSP585. The grey lines represent Pareto-optimal policies, while the red
 567 and blue lines indicate the solutions with the highest guarantee rate and maximum hydropower

568 generation, respectively, and the black line indicates the historical operating pattern. Each axis
569 represents an objective, with the optimal direction oriented upwards.

570

571 4.5 Limitations, uncertainties, and implications

572 While the proposed framework provides a data-driven way to represent reservoir-regulated
573 hydrological droughts under future climate scenarios, several limitations and sources of
574 uncertainty should be explicitly acknowledged. These aspects are important for interpreting the
575 robustness, scope, and broader applicability of our results.

576 **I) Possible non-stationarity of the operating environment and limited climate-model**
577 **sampling.** In our framework, the physics-guided LSTM module learns reservoir operating
578 behavior from historical conditions and is subsequently applied to the reference and future periods.
579 This implicitly assumes that the governing operating objectives and constraints remain broadly
580 stable, and that the learned decision logic is transferable across time. Our previous analyses
581 indicate that, for the case investigated here, the reservoir-regulated hydrological response exhibits
582 relatively stable patterns over multi-decadal timescales, supporting the feasibility of using a
583 surrogate model to represent the whole-period operational behavior (He et al., 2023). However,
584 such consistency is case-specific and may not hold in other basins where human interventions are
585 stronger; therefore, caution is warranted when applying the proposed approach beyond the study
586 basin. In addition, future projections are driven by a limited set of climate forcings (five ISIMIP3b
587 GCMs), which may not fully span plausible hydroclimatic trajectories and extremes, thereby
588 constraining the uncertainty range of the simulated drought responses. Key extensions include
589 stress-testing surrogate transferability under plausible operational changes and quantifying
590 climate-forcing uncertainty using a larger GCM ensemble.

591 **II) Sensitivity of drought inferences to calibration choices and single-basin LSTM**
592 **training.** Simulated hydrological drought characteristics can depend on the objective function

593 adopted during model calibration (Knoben et al., 2019). In this study, calibration primarily relied
594 on *NSE*, which tends to emphasize high-flow conditions at the expense of low-flow fidelity. This
595 may affect drought assessments because, at the low-flow end of the flow regime (i.e., high
596 exceedance probabilities), streamflow deficits play a dominant role in shaping drought onset,
597 persistence, and severity. Consistent with this concern, the FDCs in Figures 5(b) and 5(d) indicate
598 a systematic high bias in low flows, implying that the absolute magnitude of drought intensity
599 derived from simulated streamflow may be underestimated. Although our subsequent analyses
600 focus on relative changes with respect to the ISIMIP3b_ref baseline, this sensitivity should be
601 acknowledged. A more drought-facing calibration setup, e.g., low-flow-oriented objectives (log-
602 transformed *NSE*), provides a direct path to reduce this sensitivity.

603 Beyond calibration, the physics-guided LSTM surrogate in our framework is trained using
604 data from a single reservoir-regulated basin, which constrains the training envelope to the
605 historical range of hydroclimatic and operational conditions represented in that system. This design
606 choice was primarily motivated by limited access to harmonized reservoir operation records across
607 regulated basins and by our focus on the target reservoir-regulated basin. Recent guidance for
608 rainfall–runoff LSTM modeling highlights that single-basin training can limit generalization,
609 particularly for extreme events, whereas multi-basin training on hydrologically diverse data is
610 often more robust (Kratzert et al., 2024). As data availability permits, a natural extension is to
611 conduct multi-basin (or multi-reservoir-system) training followed by fine-tuning to the target basin,
612 and to explicitly evaluate how such training affects the simulation of drought-relevant low flows
613 and extreme drought events.

614 **III) Limitations in the design of our optimized operating policy.** Many reservoir
615 optimization studies remain at a preliminary stage, where operating rules are optimized using

616 historical observations and then deemed superior based solely on comparisons with historical
617 performance. Although the observed historical operation, which is shaped by complex real-world
618 objectives and constraints, is Pareto-dominated in the objective space of annual average
619 hydropower generation and power-generation guarantee rate (Figure 10), it is not necessarily
620 outperformed by most Pareto-optimal policies under future scenarios, particularly in terms of
621 guarantee rate and drought frequency (Figure 11). In addition, a common challenge with Pareto-
622 optimal solution sets is selecting a single implementable policy. By benchmarking the future
623 performance of candidate Pareto solutions against the historical operating policy, we found that
624 the reliability-oriented solution, that is, the one with the highest guarantee rate, performs better
625 than the historical operating policy across most future scenarios, except for drought frequency,
626 whereas the hydropower-optimal solution does not show consistent advantages. Moreover,
627 hydropower generation is broadly similar across the Pareto set in future periods, suggesting limited
628 differentiation in this metric. Together, these findings suggest that, for the Ankang system, the
629 reliability-oriented solution is a more defensible candidate for implementation. Nevertheless, our
630 drought-focused analysis optimized policies primarily for hydropower generation and guarantee
631 rate and then directly applied them to future scenarios to examine trade-offs with hydrological
632 drought mitigation. This indicates scope for further improvements in drought mitigation
633 performance. Future work could incorporate drought-event characteristics as explicit objectives or
634 constraints, and consider other human interventions (e.g., inter-basin water transfers and
635 urbanization) to better bracket plausible drought-mitigation pathways under changing conditions
636 (Wu et al., 2023; Firoz et al., 2018).

637

638 **5 Conclusions**

639 By performing a simultaneous simulation of a LSTM-based reservoir inflow model and a
640 physics-guided reservoir operation model, this study achieved a fully automated ML projection of
641 river streamflow changes over the UHRB under different future scenarios and used it to project
642 the associated hydrological drought. Climate change and reservoir operation were successively
643 considered in the projections to reveal their different roles. Additionally, the trade-off between
644 future hydrological droughts and operating benefits (i.e., hydropower generation and power
645 generation guarantee rate) was investigated by optimizing the reservoir operating policies. The
646 main findings are summarized as follows:

647 1. A reasonable LSTM-based model architecture is recommended for hydrological
648 simulation in the reservoir-regulated region. If the historical meteorological simulation of
649 ISIMIP3b is used instead of hydrological observations, it can still reflect the inflow and release of
650 Ankang Reservoir as well as changes in reservoir storage. This demonstrates the feasibility of
651 projecting future streamflow and associated hydrological droughts using ML approaches.

652 2. Future climate change over the UHRB tends to reduce natural streamflow and exacerbate
653 hydrological droughts, especially in the far-future period (2071-2100) under the SSP585 scenario.
654 While the operation of the Ankang Reservoir can mitigate the frequency, duration, and severity of
655 short-term hydrological droughts (SSI-1 and SSI-3), it shows limited effectiveness in alleviating
656 long-term droughts (SSI-12).

657 3. Optimal reservoir operating policies at Ankang Reservoir, designed to maximize
658 hydropower generation and power generation guarantee rates, highlight clear trade-offs between
659 hydrological drought risk and hydropower benefits, especially in the near-future period (2031-
660 2060). Compared to the historically derived policy, these optimal strategies yield higher

661 hydropower benefits but may also lead to increased drought frequency. The finding that a small
662 subset of optimal policies consistently delivers robust performance across multiple indicators
663 under plausible future scenarios underscores its potential to enhance regional water resources
664 management under climate change.

665

666 **Declaration of Competing Interest**

667 The authors declare that they have no known competing financial interests or personal
668 relationships that could have appeared to influence the work reported in this paper.

669

670 **Data availability**

671 The code that supports the findings of this study is available from the corresponding author
672 upon reasonable request. The ISIMIP3b data used in producing this paper are available at
673 <https://data.isimip.org/search/tree/ISIMIP3b/InputData/>. Observed streamflow data are available
674 from the Bureau of Hydrology of the Yangtze Water Resources Commission of China
675 (<https://www.cjh.com.cn>).

676

677 **Author contribution**

678 YG, KC and SH designed the study. SH, SS, and YL developed the models, with SH and LZ
679 implementing them. SH drafted the manuscript in close collaboration with YG, SS, YL contributed
680 to the data curation. Throughout the study period, all the authors engaged in discussions regarding
681 the results, provided critical feedback, and approved the final version of the paper.

682

683 **Supplement**

684 The supplement related to this article is available.

685

686 **Financial support**

687 This research has been supported by the National Key Research and Development Program
688 of China (2023YFC3209502) and National Natural Science Foundation of China (U2340217 and
689 42577102).

690 **References**

- 691 Abadi, M., Barham, P., Chen, J., Chen, Z., and Davis, A.: TensorFlow: a system for large-scale machine learning In:
692 Proceedings of the 12th USENIX conference on Operating Systems Design and Implementation. USENIX
693 Association, Savannah, GA, USA, 265-283, 2016.
- 694 Arsenault, R., Martel, J.-L., Brunet, F., Brisette, F., and Mai, J.: Continuous streamflow prediction in ungauged
695 basins: long short-term memory neural networks clearly outperform traditional hydrological models, *Hydrol Earth
696 Syst Sc*, 27, 139-157, 10.5194/hess-27-139-2023, 2023.
- 697 Bertoni, F., Castelletti, A., Giuliani, M., and Reed, P. M.: Discovering Dependencies, Trade-Offs, and Robustness in
698 Joint Dam Design and Operation: An Ex-Post Assessment of the Kariba Dam, *Earth's Future*, 7, 1367-1390,
699 10.1029/2019ef001235, 2019.
- 700 Brunner, M. I.: Reservoir regulation affects droughts and floods at local and regional scales, *Environ Res Lett*, 16,
701 124016, 10.1088/1748-9326/ac36f6, 2021.
- 702 Chai, Y., Yue, Y., Slater, L. J., Yin, J., Borthwick, A. G. L., Chen, T., and Wang, G.: Constrained CMIP6
703 projections indicate less warming and a slower increase in water availability across Asia, *Nat Commun*, 13, 4124,
704 10.1038/s41467-022-31782-7, 2022.
- 705 Chang, L., Cheng, L., Zhang, L., Han, D., Zhang, J., and Liu, P.: Remote sensing-based high-resolution reservoir
706 drought index for identifying the occurrence and propagation of hydrological droughts in a large river basin, *Remote
707 Sensing of Environment*, 328, 114859, 10.1016/j.rse.2025.114859, 2025.
- 708 Cheng, H., Wang, T., and Yang, D.: Quantifying the Regulation Capacity of the Three Gorges Reservoir on Extreme
709 Hydrological Events and Its Impact on Flow Regime in a Changing Climate, *Water Resour Res*, 60,
710 e2023WR036329, 10.1029/2023wr036329, 2024.
- 711 Cui, Z., Zhou, Y., Guo, S., Wang, J., and Xu, C.-Y.: Effective improvement of multi-step-ahead flood forecasting
712 accuracy through encoder-decoder with an exogenous input structure, *J Hydrol*, 609, 127764,
713 10.1016/j.jhydrol.2022.127764, 2022.
- 714 Culley, S., Noble, S., Yates, A., Timbs, M., Westra, S., Maier, H. R., Giuliani, M., and Castelletti, A.: A bottom-up
715 approach to identifying the maximum operational adaptive capacity of water resource systems to a changing climate,
716 *Water Resour Res*, 52, 6751-6768, 10.1002/2015wr018253, 2016.
- 717 Dams, C. N. C. o. L.: Ankang hydropower project. Beijing: Chinese National Committee on Large Dams (in
718 Chinese), 2011.
- 719 Deb, K., Pratap, A., Agarwal, S., and Meyarivan, T.: A fast and elitist multiobjective genetic algorithm: NSGA-II,
720 *Ieee T Evolut Comput*, 6, 182-197, 10.1109/4235.996017, 2002.
- 721 Eriyagama, N., Smakhtin, V., and Udumulla, L.: How much artificial surface storage is acceptable in a river basin
722 and where should it be located: A review, *Earth-Science Reviews*, 208, 103294, 10.1016/j.earscirev.2020.103294,
723 2020.
- 724 Firoz, A. B. M., Nauditt, A., Fink, M., and Ribbe, L.: Quantifying human impacts on hydrological drought using a
725 combined modelling approach in a tropical river basin in central Vietnam, *Hydrol Earth Syst Sc*, 22, 547-565,
726 10.5194/hess-22-547-2018, 2018.
- 727 G. Ribeiro Neto, G., Kchouk, S., Melsen, L. A., Cavalcante, L., Walker, D. W., Dewulf, A., Costa, A. C., Martins,
728 E. S. P. R., and van Oel, P. R.: HESS Opinions: Drought impacts as failed prospects, *Hydrol Earth Syst Sc*, 27,
729 4217-4225, 10.5194/hess-27-4217-2023, 2023.

730 García-Feal, O., González-Cao, J., Fernández-Nóvoa, D., Astray Dopazo, G., and Gómez-Gesteira, M.: Comparison
731 of machine learning techniques for reservoir outflow forecasting, *Natural Hazards and Earth System Sciences*, 22,
732 3859-3874, 10.5194/nhess-22-3859-2022, 2022.

733 Gu, L., Chen, J., Yin, J., Xu, C. Y., and Zhou, J.: Responses of precipitation and runoff to climate warming and
734 implications for future drought changes in China, *Earth's Future*, 8, e2020EF001718, 10.1029/2020ef001718, 2020.

735 Gudmundsson, L., Boulange, J., Do, H. X., Gosling, S. N., Grillakis, M. G., Koutroulis, A. G., Leonard, M., Liu, J.,
736 Müller Schmied, H., Papadimitriou, L., Pokhrel, Y., Seneviratne, S. I., Satoh, Y., Thiery, W., Westra, S., Zhang, X.,
737 and Zhao, F.: Globally observed trends in mean and extreme river flow attributed to climate change, *Science*, 371,
738 1159-1162, 10.1126/science.aba3996, 2021.

739 Hanasaki, N., Kanae, S., and Oki, T.: A reservoir operation scheme for global river routing models, *J Hydrol*, 327,
740 22-41, 10.1016/j.jhydrol.2005.11.011, 2006.

741 He, S., Chen, K., Liu, Z., and Deng, L.: Exploring the impacts of climate change and human activities on future
742 runoff variations at the seasonal scale, *J Hydrol*, 619, 129382, 10.1016/j.jhydrol.2023.129382, 2023.

743 He, S., Li, B., Li, Q., Zheng, H., and Chen, Y.: Refining hydropower operation by dynamic control of cascade
744 reservoir water levels with flood season segmentation, *Energy*, 314, 134156, 10.1016/j.energy.2024.134156, 2025.

745 He, S., Guo, S., Zhang, J., Liu, Z., Cui, Z., Zhang, Y., and Zheng, Y.: Multi-objective operation of cascade
746 reservoirs based on short-term ensemble streamflow prediction, *J Hydrol*, 610, 127936,
747 10.1016/j.jhydrol.2022.127936, 2022.

748 Ho, S. Q.-G. and Ehret, U.: Is drought protection possible without compromising flood protection? Estimating the
749 potential dual-use benefit of small flood reservoirs in southern Germany, *Hydrol Earth Syst Sc*, 29, 2785-2810,
750 10.5194/hess-29-2785-2025, 2025.

751 Hochreiter, S.: The Vanishing Gradient Problem During Learning Recurrent Neural Nets and Problem Solutions,
752 *International Journal of Uncertainty, Fuzziness and Knowledge-Based Systems*, 06, 107-116,
753 10.1142/s0218488598000094, 1998.

754 Hochreiter, S. and Schmidhuber, J.: Long short-term memory, *Neural Computation*, 9, 1735-1780,
755 10.1162/neco.1997.9.8.1735, 1997.

756 Hosking, J. R. M.: L-Moments: Analysis and estimation of distributions using linear combinations of order statistics,
757 *Journal of the Royal Statistical Society: Series B (Methodological)*, 52, 105-124, 10.1111/j.2517-
758 6161.1990.tb01775.x, 1990.

759 Huang, J., Wu, W., Maier, H. R., Hughes, J., Wang, Q. J., and Cao, Y.: Comprehensive framework for long-term
760 reservoir management under deep uncertainty, *Environ Modell Softw*, 195, 106740, 10.1016/j.envsoft.2025.106740,
761 2026.

762 Huang, J., Sangiorgio, M., Wu, W., Maier, H. R., Wang, Q. J., Hughes, J., and Castelletti, A.: Solving the robustness
763 puzzle: The joint impact of optimization approach, robustness metrics, and scenarios on water resources
764 management under deep uncertainty, *Journal of Environmental Management*, 373, 123540,
765 10.1016/j.jenvman.2024.123540, 2025.

766 IPCC: The Physical Science Basis. Contribution of Working Group I to the Sixth Assessment Report of the
767 Intergovernmental Panel on Climate Change. Cambridge University Press, 2021.

768 Ji, P., Yuan, X., and Jiao, Y.: Future hydrological drought changes over the upper Yellow River basin: The role of
769 climate change, land cover change and reservoir operation, *J Hydrol*, 617, 129128, 10.1016/j.jhydrol.2023.129128,
770 2023.

771 Jin, H., Willems, P., Chen, X., and Liu, M.: Nonstationary flood and its influencing factors analysis in the Hanjiang
772 River Basin, China, *J Hydrol*, 625, 129994, 10.1016/j.jhydrol.2023.129994, 2023.

773 Kang, S., Yin, J., Gu, L., Yang, Y., Liu, D., and Slater, L.: Observation-constrained projection of flood risks and
774 socioeconomic exposure in China, *Earth's Future*, 11, e2022EF003308, 10.1029/2022ef003308, 2023.

775 Kheyruri, Y., Sharafati, A., and Neshat, A.: The socioeconomic impact of severe droughts on agricultural lands over
776 different provinces of Iran, *Agricultural Water Management*, 289, 108550, 10.1016/j.agwat.2023.108550, 2023.

777 Kingma, D. P. and Ba, J.: Adam: a method for stochastic optimization. arXiv:1412.6980 [cs.LG]. 2014.

778 Knoben, W. J. M., Freer, J. E., and Woods, R. A.: Technical note: Inherent benchmark or not? Comparing Nash–
779 Sutcliffe and Kling–Gupta efficiency scores, *Hydrol Earth Syst Sc*, 23, 4323-4331, 10.5194/hess-23-4323-2019,
780 2019.

781 Kratzert, F., Gauch, M., Klotz, D., and Nearing, G.: HESS Opinions: Never train a Long Short-Term Memory
782 (LSTM) network on a single basin, *Hydrol Earth Syst Sc*, 28, 4187-4201, 10.5194/hess-28-4187-2024, 2024.

783 Lange, S.: Trend-preserving bias adjustment and statistical downscaling with ISIMIP3BASD (v1.0), *Geosci. Model
784 Dev.*, 12, 3055-3070, 10.5194/gmd-12-3055-2019, 2019.

785 Levey, J. R. and Sankarasubramanian, A.: Is Reservoir Storage Effectively Utilized in the Southeastern US? A
786 Regional Assessment to Improve Water Supply Availability Considering Potential Storage and Flood Scenarios,
787 *Earth's Future*, 13, e2024EF005176, 10.1029/2024ef005176, 2025.

788 Liu, J., Yuan, X., Zeng, J., Jiao, Y., Li, Y., Zhong, L., and Yao, L.: Ensemble streamflow forecasting over a cascade
789 reservoir catchment with integrated hydrometeorological modeling and machine learning, *Hydrol Earth Syst Sc*, 26,
790 265-278, 10.5194/hess-26-265-2022, 2022.

791 Longyang, Q. and Zeng, R.: A Hierarchical Temporal Scale Framework for Data-Driven Reservoir Release
792 Modeling, *Water Resour Res*, 59, e2022WR033922, 10.1029/2022wr033922, 2023.

793 Özdoğan-Sarıkoç, G., Sarıkoç, M., Celik, M., and Dadaser-Celik, F.: Reservoir volume forecasting using artificial
794 intelligence-based models: Artificial Neural Networks, Support Vector Regression, and Long Short-Term Memory,
795 *J Hydrol*, 616, 128766, 10.1016/j.jhydrol.2022.128766, 2023.

796 Quinn, J. D., Reed, P. M., Giuliani, M., and Castelletti, A.: What is controlling our control rules? Opening the black
797 box of multireservoir operating policies using time-varying sensitivity analysis, *Water Resour Res*, 55, 5962-5984,
798 10.1029/2018wr024177, 2019.

799 Rehana, S. and Rajesh, M.: Assessment of impacts of climate change on Indian riverine thermal regimes using
800 hybrid deep learning methods, *Water Resour Res*, 59, e2021WR031347, 10.1029/2021wr031347, 2023.

801 Satoh, Y., Yoshimura, K., Pokhrel, Y., Kim, H., Shiogama, H., Yokohata, T., Hanasaki, N., Wada, Y., Burek, P.,
802 Byers, E., Schmied, H. M., Gerten, D., Ostberg, S., Gosling, S. N., Boulange, J. E. S., and Oki, T.: The timing of
803 unprecedented hydrological drought under climate change, *Nat Commun*, 13, 3287, 10.1038/s41467-022-30729-2,
804 2022.

805 Shukla, S. and Wood, A. W.: Use of a standardized runoff index for characterizing hydrologic drought, *Geophysical*
806 *Research Letters*, 35, L02405, 10.1029/2007gl032487, 2008.

807 Smith, K. A., Barker, L. J., Tanguy, M., Parry, S., Harrigan, S., Legg, T. P., Prudhomme, C., and Hannaford, J.: A
808 multi-objective ensemble approach to hydrological modelling in the UK: an application to historic drought
809 reconstruction, *Hydrol Earth Syst Sc*, 23, 3247-3268, 10.5194/hess-23-3247-2019, 2019.

810 Solanki, H., Vegad, U., Kushwaha, A., and Mishra, V.: Improving Streamflow Prediction Using Multiple
811 Hydrological Models and Machine Learning Methods, *Water Resour Res*, 61, e2024WR038192,
812 10.1029/2024wr038192, 2025.

813 Sun, J., Chen, W., Hu, B., Xu, Y. J., Zhang, G., Wu, Y., Hu, B., and Song, Z.: Roles of reservoirs in regulating basin
814 flood and droughts risks under climate change: Historical assessment and future projection, *Journal of Hydrology:*
815 *Regional Studies*, 48, 101453, 10.1016/j.ejrh.2023.101453, 2023.

816 Tran, H., Zhou, T., Tan, Z., Fang, Y., and Ruby Leung, L.: Improving the prediction of daily reservoir releases over
817 the CONUS using conditioned LSTM, *J Hydrol*, 661, 133750, 10.1016/j.jhydrol.2025.133750, 2025.

818 Vicente-Serrano, S. M., Lopez-Moreno, J. I., Begueria, S., Lorenzo-Lacruz, J., Azorin-Molina, C., and Moran-
819 Tejada, E.: Accurate computation of a streamflow drought index, *Journal of Hydrologic Engineering*, 17, 318-332,
820 10.1061/(Asce)He.1943-5584.0000433, 2012.

821 Wan, W., Wang, Z., Cheng, L., Bai, Y., Wang, W., and Wang, K.: Integrating Drought Warning Water Level With
822 Analytical Hedging for Reservoir Water Supply Operation, *Water Resour Res*, 61, e2024WR038680,
823 10.1029/2024wr038680, 2025.

824 Wan, W., Zhao, J., Li, H. Y., Mishra, A., Hejazi, M., Lu, H., Demissie, Y., and Wang, H.: A holistic view of water
825 management impacts on future Droughts: A Global Multimodel Analysis, *Journal of Geophysical Research:*
826 *Atmospheres*, 123, 5947-5972, 10.1029/2017jd027825, 2018.

827 Wanders, N. and Wada, Y.: Human and climate impacts on the 21st century hydrological drought, *J Hydrol*, 526,
828 208-220, 10.1016/j.jhydrol.2014.10.047, 2015.

829 Wu, G., Chen, J., Shi, X., Kim, J. S., Xia, J., and Zhang, L.: Impacts of global climate warming on meteorological
830 and hydrological droughts and their propagations, *Earth's Future*, 10, e2021EF002542, 10.1029/2021ef002542,
831 2022.

832 Wu, J., Chen, X., Yao, H., Gao, L., Chen, Y., and Liu, M.: Non-linear relationship of hydrological drought
833 responding to meteorological drought and impact of a large reservoir, *J Hydrol*, 551, 495-507,
834 10.1016/j.jhydrol.2017.06.029, 2017.

835 Wu, Y., Sun, J., Hu, B., Xu, Y. J., Rousseau, A. N., and Zhang, G.: Can the combining of wetlands with reservoir
836 operation reduce the risk of future floods and droughts?, *Hydrol Earth Syst Sc*, 27, 2725-2745, 10.5194/hess-27-
837 2725-2023, 2023.

838 Yang, S., Yang, D., Chen, J., and Zhao, B.: Real-time reservoir operation using recurrent neural networks and
839 inflow forecast from a distributed hydrological model, *J Hydrol*, 579, 124229, 10.1016/j.jhydrol.2019.124229, 2019.

840 Yevjevich, V.: An objective approach to definitions and investigation of continental hydrologic droughts, Hydrology
841 Paper23. Fort Collins, Colorado State U., 1967.

842 Yun, X., Tang, Q., Sun, S., and Wang, J.: Reducing Climate Change Induced Flood at the Cost of Hydropower in
843 the Lancang-Mekong River Basin, Geophysical Research Letters, 48, e2021GL094243, 10.1029/2021gl094243,
844 2021a.

845 Yun, X., Tang, Q., Li, J., Lu, H., Zhang, L., and Chen, D.: Can reservoir regulation mitigate future climate change
846 induced hydrological extremes in the Lancang-Mekong River Basin?, Sci Total Environ, 785,
847 10.1016/j.scitotenv.2021.147322, 2021b.

848 Zhang, X., Song, Z., Zhou, T., Wang, D., Wang, Y., and Liu, P.: Reservoir operation strategies to mitigate
849 hydrological drought effects along the middle and lower reaches of the Yangtze River, Journal of Hydrology:
850 Regional Studies, 58, 102204, 10.1016/j.ejrh.2025.102204, 2025.

851 Zheng, Y., Liu, P., Cheng, L., Xie, K., Lou, W., Li, X., Luo, X., Cheng, Q., Han, D., and Zhang, W.: Extracting
852 operation behaviors of cascade reservoirs using physics-guided long-short term memory networks, Journal of
853 Hydrology: Regional Studies, 40, 101034, 10.1016/j.ejrh.2022.101034, 2022.

854 Zhou, Z., Shi, H., Fu, Q., Ding, Y., Li, T., and Liu, S.: Investigating the propagation from meteorological to
855 hydrological drought by introducing the nonlinear dependence with directed information transfer index, Water
856 Resour Res, 57, e2021WR030028, 10.1029/2021wr030028, 2021.

857